AMERICAN UNIVERSITY OF BEIRUT

NATURAL CONVECTION IN AN OPEN-ENDED ISOTHERMALLY-HEATED THREE-DIMENSIONAL BUILDING SHAFT

by
MARAM RIAD AMMAR

A thesis
submitted in partial fulfillment of the requirements
for the degree of Master of Engineering
to the Department of Mechanical Engineering
of Maroun Semaan Faculty of Engineering and Architecture
at the American University of Beirut

Beirut, Lebanon
May 2022

AMERICAN UNIVERSITY OF BEIRUT

NATURAL CONVECTION IN AN OPEN-ENDED ISOTHERMALLY-HEATED THREE-DIMENSIONAL BUILDING SHAFT

by

MARAM RIAD AMMAR

Approved by:

Prof. Issam Lakkis, Professor — Advisor

Mechanical Engineering

Prof. Fadl Moukalled, Professor — Member of Committee

Mechanical Engineering

Prof. Aram Yeretzian, Assistant Professor — Member of Committee

Architecture and Design

Aram Yeretzian

Digitally signed by Aram Yeretzian
DN: cn=Aram Yeretzian, o=American University of Beirut, ou, email=ay10@aub.edu.lb, c=LB
Date: 2022.05.10 09:33:23 +03'00'

Date of thesis defense: April 29, 2022

AMERICAN UNIVERSITY OF BEIRUT

THESIS RELEASE FORM

Student Name: Ammar (Last) Maram (First) Riad (Middle)

I authorize the American University of Beirut, to: (a) reproduce hard or electronic copies of my thesis; (b) include such copies in the archives and digital repositories of the University; and (c) make freely available such copies to third parties for research or educational purposes

_X_ **As of the date of submission of my thesis**

___ **After 1 year from the date of submission of my thesis .**

___ **After 2 years from the date of submission of my thesis .**

___ **After 3 years from the date of submission of my thesis .**

Maram Ammar Digitally signed by Maram Ammar DN: cn=Maram Ammar, o, ou, email=mra56@mail.aub.edu, c=LB Date: 2022.05.10 10:05:50 +03'00'

Signature

May 10, 2022

Date

Acknowledgements

First and foremost, I would like to thank God who drew this path for me and who had better plans for me than I had for myself.

I would like to express my sincere gratitude to my family who has stood by me and supported me unconditionally. Given the dire conditions we have survived in Lebanon, my mother and father did everything in their power to prevent anything from hindering my progress. My sisters constantly provided me with spiritual support especially during my hard times. I am truly blessed to have you as my family, my backbone.

I am deeply grateful to my advisor, Professor Issam Lakkis, who has opened doors for me and given me opportunities I never dreamed of. I wholeheartedly thank him for all that he has taught me from his immense knowledge and expertise. His motivation and patience stirred up my interest in research. I couldn't have imagined a better advisor to guide me through my study.

I would also like to offer my warmest thanks to Professor Fadl Moukalled, who is a member of my thesis committee. Professor Moukalled was never reluctant in providing me with the advice I needed to proceed with my work, and I truly appreciate his insightful comments and suggestions to my project.

I would like to extend my gratitude to Dr. Imane Khalil, with whom I have collaborated on a different project. With her support, all that I learned in this project was directly reflected on my thesis. I am genuinely thankful to her kindness, generosity and her motivation.

Finally, I would like to thank Professor Aram Yeretzian for coadvising this project and my lab colleagues and friends for their help and support.

Abstract
of the Thesis of

Maram Riad Ammar for Master of Engineering
Major: Applied Energy

Title: Natural convection in an open-ended isothermally-heated three-dimensional building shaft

The increased rates of mortality and morbidity in urban areas have been associated with increased levels of pollutant concentration. This study aims at employing natural convection effects to ventilate urban street canyons passively. This is a numerical study which investigates turbulent three-dimensional natural convection flows in isothermally-heated open-ended building shafts. Five shaft size values $\{1,\ 2,\ 3,\ 4,\ 5\}$ m and six temperature difference values $\{5,\ 10,\ 15,\ 20,\ 25,\ 30\}$ °C are taken. Air is modeled as an ideal gas, and the $SSTk-\omega$ model is used for turbulence modeling. The maximum wall y^+ value among all cases is 7.2. Results include streamline plots at the entrance of the shaft, average velocity profiles at different elevations, wall heat flux rate profiles, centerline velocity profiles, isotherm plots at different elevations, mass flow rate contours and a plot on the mass flow rate and total heat rate emitted by the walls. Flow separation occurs in all cases. The mass flow rate generated in the shaft ranges between 1.05-23.53 kg/s, and the total heat rate emitted by the walls ranges between 1.67-91.47 kW.

Table of Contents

Illustrations

Tables

Abbreviations

$\mathtt{Nu}$	Nusselt Number
$\mathtt{Gr}$	Grashoff Number
$\mathtt{Pr}$	Pandtl Number
$\mathtt{Ra}$	Rayleigh Number
$\mathtt{Ra}_m$	Modified Rayleigh Number
ρ	Density ($\frac{\mathrm{kg}}{\mathrm{m}^3}$)
g	gravitational acceleration $\frac{\mathrm{m}}{\mathrm{s}^2}$
β	Thermal expansion coefficient $\frac{1}{\mathrm{K}}$
b	Shaft width (m)
T	Temperature (K)
μ	Dynamic viscosity $\frac{\mathrm{kg}}{\mathrm{ms}}$
RANS	Reynolds-averaged Navier Stokes
t	Time
$\vec{u}$	Velocity vector
p	pressure
c_p	Constant pressure specific heat
λ	Thermal conductivity
Φ	Viscous Dissipation
y^+	Normalized Distance to a wall
y	Normal distance to a wall
u^*	friction velocity
τ_w	Wall shear
AR	Aspect ratio
μ_t	Turbulent viscosity
λ_t	Turbulent conductivity
k	Turbulent kinetic energy
P_k^*	Turbulent energy production
ω	Specific turbulence dissipation
F_1	Blending function
$\hat{\rho}$	Dimensionless density

$\tilde{u}$	Dimensionless velocity
$\hat{p}$	Dimensionless pressure
$\hat{\mu}_t$	Dimensionless turbulent viscosity
$\hat{\lambda}$	Dimensionless thermal conductivity
$\hat{T}$	Dimensionless temperature
$\hat{\Phi}$	Dimensionless Turbulence Dissipation
$\hat{k}$	Dimensionless kinetic energy
$\hat{\omega}$	Dimensionless specific turbulence dissipation
$\hat{P}_k^*$	Dimensionless turbulent energy production
$\mathtt{Ra}_{vp}$	Rayleigh number for vertical plates
$\mathtt{Nu}_{vp}$	Nusselt Number for vertical plates
L	characteristic length of a vertical plate

Chapter 1

Introduction

The detrimental impacts of urbanization on human health and the environment have been the subject of numerous investigations. The impacts of interest in this study are related to urban overheating and degraded air quality. Aggravated outdoor thermal conditions and increased levels of pollutant concentration have been associated with increased rates of mortality and morbidity, increased energy consumption in buildings, decreased efficiency of power plants among others. [1] In 2018, the United Nations estimated that around 55% of the world population resided in urban areas, and this number is projected to increase to 68% by 2050 [2]. Consequently, it is essential to abate urban overheating and disperse pollutants at pedestrian level. In this study, we aim at employing natural convection effects to ventilate urban street canyons passively in an attempt to improve air quality in addition to outdoor conditions.

Heat transfer by natural convection is present in a wide range of applications such as cooling of electronic equipment, heating buildings passively, designing solar collectors, designing nuclear reactors, etc. The two classes into which free convection could be divided are internal and external natural convection. In the prior, the flow is confined within the boundaries of the domain, whereas in the latter, the flow surrounds a body maintained at a temperature different than the ambient temperature. In internal flows, the shape of the passage and its orientation vary from one application to another. In some applications, the passage could be rectangular, and in others it could be curved, trapezoidal, and so on.

The different factors affecting the characteristics of natural convection flows have been extensively studied in literature. Rahimi et al. [3] addressed the impact on natural convection heat transfer of changing the enclosure's geometry and the type of fluid used, while Pandey et al. [4] analyzed the effect of adding a body to the enclosure on natural convection currents. In another study, Miroshnichenko and Sheremet [5] reviewed the various methods -finite volume, finite difference, Lattice Boltzmann, experiments- that have been used by researchers to model flow fields established by

natural convection.
Natural convection in enclosures could be induced by several methods. One method is differentially heating the vertical walls of the enclosure where the temperature gradient is perpendicular to the gravitational field. Roeleveld et al. [6] investigated the buoyancy forces and Habib et al. [7] presented the velocity measurements in an asymmetrically heated open-ended vertical channel where one wall is maintained at a temperature higher than the ambient temperature, and the other is maintained lower than the ambient temperature. Mohamad et al [8] reported the average nusselt number and presented isotherm plots for the case of applying non-uniform conditions on the vertical walls. Inducing natural convection currents can also be achieved by maintaining an open-ended enclosure's vertical walls at a temperature higher than the ambient temperature as in the case of isothermally heated vertical channels. Some studies addressed natural convection in such configurations, and those include the study performed by Bodoia and Osterle, [9] who revealed that full development of the flow can be practically attained for very viscous flows. In 2005, Badr et al.[10] examined turbulent natural convection flows in vertical channels by applying isothermal and isoflux conditions. The authors presented the velocity profiles along horizontal sections in the channel. In natural convection flows, the key variable that indicates the type of the flow -laminar, transition, or turbulent- is Rayleigh number [11]. To the authors' knowledge the critical value of Rayleigh number beyond which the flow becomes turbulent is not clearly established for vertical channels and much less so for isothermally heated three-dimensional ducts. However, in a few studies [12] and [13] the flow, in a vertical channel, was considered turbulent at a Rayleigh number that exceeded 10^5.
Nusselt number (Nu) is among the key parameters that characterize the flow and give a better insight on the mode of heat transfer. Knowing that Nu is affected by several factors such as Rayleigh number, Reynolds number, fluid properties, boundary conditions and geometric parameters, many studies have reported empirical correlations that predict Nu for different flow conditions in ducts. The model presented by Sarmiento et al. [14] predicts the Nusselt number in non-circular ducts in microchannel applications. For steady laminar natural convection in an isothermally heated vertical duct, Yvanovitch et al. [15] developed a correlation of Nu for a wide range of duct shapes and aspect ratios. For forced laminar convection flows, Muzychka and Yovanovich [16] established a model for Nu that is valid for Pr values greater than one. Other studies reported the variation of the Nu profile. In the studies where isothermal conditions were employed, such as [17], [18] and [19], the authors reported that the local value of the Nusselt number decreases with height. Such a profile of Nu is evident when the flow is laminar where a thermal boundary layer near the walls is created. The thermal boundary layer acts as thermal resistance, which reduces heat transfer from the walls to the ambient. Another important parameter in natural convection

flows is the Grashoff number (Gr) which is the ratio of the buoyancy forces to viscous ones. Naylor et al. [20] and Lakkis and Moukalled. [19] both reported the presence of a recirculation zone at the entrance of the channel when the Grashoff number is sufficiently high.
The characteristics of the flow are strongly affected by values of Prandtl number (Pr), which is the ratio of the kinematic viscosity to the thermal diffusivity. In 2014, Gangawane et al. [21] investigated the impact of Prandtl and Rayleigh (Ra) numbers on the natural convection flow in a two-dimensional open ended rectangular cavity. Their geometric model consists of a vertical wall that is partially heated and connected to two adiabatic vertical walls. The results reported demonstrated a higher clustering of isotherms near the heated walls with an increase in Pr and/or Ra number values. The authors associated this with the fact that lower Prandtl numbers promote heat conduction which results in a more uniform distribution of isotherms in the cavity. This is in agreement with the results of another study conducted by Moukalled and Lakkis [22] who noted that increasing Ra strengthens convection effects and attenuates conduction effects leading to a non-uniform distribution of isotherms. Sefcik et al. [23], investigated the effects on natural convection heat transfer of the size of two vents located at the entrance and exit of a duct. Isothermal conditions are applied on one wall, while adiabatic conditions are applied on the other walls. The results of this study revealed the absence of a recirculation zone when the vents' width is equal to the duct's width. Moreover, the authors reported that Nu increases significantly in the region where recirculation occurs and decreases monotonously with height, for the cases when the vents' width is smaller than the duct's width. Furthermore, the study reported by Straatman et al. [24] showed improvement in the overall heat transfer in an isothermally heated channel as a consequence of adding two adiabatic extensions at the outlet. Moreover, Zamora and Kaiser[25] conducted a parametric study to optimize the wall to wall spacing in a solar chimney. The geometric model is a two-dimensional channel exposed to the interior of the building on its bottom-end and to the surrounding on its upper-end. The parameters that were varied are the channel's aspect ratio and Rayleigh number. The optimum wall to wall ratio was determined according to the optimal values of the Nusselt number and mass flow rate in the channel. Isothermal and isoflux heating conditions were imposed on the channel's walls. The generated results indicated that the optimum wall to wall spacing yielding an optimum Nusselt number is different than that yielding an optimum mass flow rate.

Even though many studies have been conducted on natural convection heat transfer in channels, the investigation of buoyancy-driven turbulent flow of air in an isothermally heated open-ended building shaft remains limited. The objectives of this study are to (1) investigate the characteristics of turbulent three-dimensional natural convection airflow in an isothermally heated open-ended shaft (2) perform a parametric

study to assess how the shaft size and temperature difference, between the walls and the ambient, affect the mass flow rate of air and the overall heat emitted by the walls (3) establish a correlation that predicts the $\mathtt{Nu}$ as a function of modified Rayleigh number ($\mathtt{Ra}_{\mathrm{m}}$).

This thesis starts with an introduction describing the motivation behind the study, findings of previous studies, and the objectives of the investigation. Then we briefly describe the geometric parameters, numerical and physical settings of the considered configuration. This is followed by expressing the governing equations in dimensional and non-dimensional forms. In the results section, we analyze the velocity streamlines at the entrance of the shaft, and the velocity profiles at different cross sections in the shaft. We also present the variation of the wall heat flux rate with height and the temperature contours at three elevations. In addition to displaying the variation of mass flow rate and total wall heat rate as a function of temperature difference, we provide a correlation between Nusselt and modified Rayleigh numbers. This is followed by validating our results and describing some limitations in our study. The thesis closes with a conclusion that recapitulates our main findings.

Chapter 2

Methods

2.1 Problem Description

2.1.1 *Geometry*

Our geometric model, presented in Figure 2.1, consists of a building whose length, width and height are 25m × 25m × 36m respectively. It comprises an open ground floor and an open-ended central square shaft. The heights of the ground floor and the shaft are 4 m and 32 m respectively. The five geometric cases covered in this study are displayed in Figure 2.1a . Taking advantage of the symmetry of our model, our computational domain consists of one fourth of the fluid domain that surrounds the building. The side boundaries of the fluid domain are taken 150 m away from the center of the shaft, and the upper boundary is taken to be at 284 m from the building's roof as depicted in Figure 2.1b.

2.1.2 *Mesh*

The geometric discretization of the model is a process in which the continuous domain is divided into a finite number of discrete elements that constitute the mesh. This process is an integral part in the numerical studies of fluid and heat transfer problems, and in some cases it is the most time consuming part. There are three types of grids that can be used to spatially discretize the domain, and those are structured, unstructured and hybrid meshes. In general, structured meshes consist of regular elements such as quadrilaterals (2D) or cuboids (3D), and unstructured meshes consist of triangles (2D) or tetrahedral elements (3D). The choice of the mesh type is typically based on several considerations such as accuracy, computational cost and time needed to generate the mesh. The merits of structured meshes include better accuracy, improved convergence, and lower memory usage. Moreover, structured

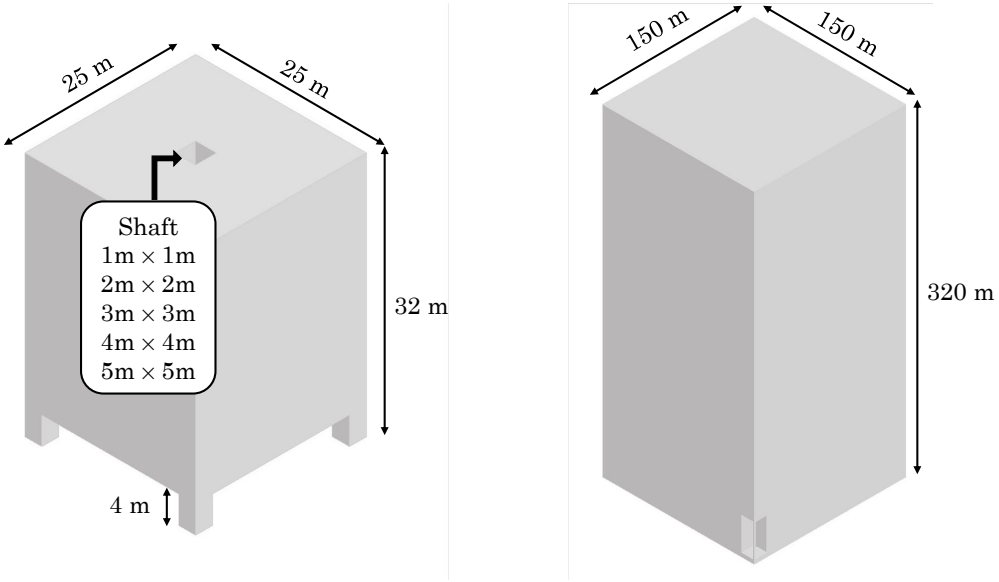

(a) Building's dimensions

(b) One fourth of the fluid domain

Figure 2.1: Geometric model

meshes are less sensitive to elongation than unstructured ones[26]. As for their shortcomings, structured meshes take significantly more time to be generated, and they are inapplicable in the discretization of complicated geometries. This compels the user to resort to unstructured or hybrid meshes.
The quality of the mesh is mainly determined by three factors, and those are accuracy, efficiency and the degree of complexity of the problem being studied. [27] Accuracy corresponds to the ability of generating a solution with the highest possible fidelity to the underlying physics. Efficiency corresponds to the ability of the mesh to generate an accurate solution with the minimum computational cost. Degree of complexity of the problem is contingent on the results in which the user is interested and their employability. In other words, for studies that aim at modeling and understanding the physical processes of some phenomenon, the mesh constraints are tighter and more stringent than those imposed on studies performed for design purposes [28]. The criteria of mesh quality assessment are contentious and have initiated much debate on its metrics. In his study, Knupp shed the light on the importance of looking at not only geometry based metrics but also solution dependent ones.
Geometry-based metrics depend on the geometric characterisctics and interaction of the cells that constitute the mesh, whereas solution-based metrics depend on the discretization error of a simulation. The utility of geometry-based metrics lies in allowing the user to detect defective meshes and take a priori measures to improve them before

running the simulation. On the other hand, solution-dependent metrics, calculated after the simulation is complete, allow the user to generate grid-independent solutions that represent the underlying physics of the problem. Some of the geometry-based metrics users traditionally report include the aspect ratio and skewness. The prior is a measure of the elongation of an element, and the latter is a measure of the deviation of a cell from its ideal shape (equi-angular shape). In general, it is recommended that the aspect ratio be close to one and the skewness be close to zero. However, there is no clear threshold value for those metrics as noted by Knupp, who pointed out that the threshold values of traditional mesh quality metrics lack mathematical-based justification and are selected arbitrarily based on the user's judgement [27]. For instance, large aspect ratios are inevitable in studies investigating highly complicated physical processes such as turbulent flows. Such flows necessitate clustering of elements near the walls to capture the sharp gradients (typically in one direction) of physical properties in the boundary layer, and as such the elements near the walls will be more elongated than those far away. In short, having aspect ratios (or other geometry-based metrics) that deviate, to some acceptable degree, from what is traditionally reported does not necessarily compromise the quality of the mesh if we are to look at accuracy, efficiency and degree of complexity of the problem.
Solution dependent metrics include the maximum wall y^+ value and the grid convergence index. The prior corresponds the normalized distance of the first grid point from the wall, and the latter is an uncertainty estimator that is based on the Richardson extrapolation scheme developed by Roach [29]. Calculating the grid convergence index necessitates generating three grids for each case and running simulations for the three grids. Running 90 simulations is beyond the scope of this study and as such, the solution-dependent metrics will be limited to the maximum wall y^+ value of all the cases covered.
The y^+ value of a grid point is calculated according to Equation 2.1:

$$y^+ = \frac{y}{\nu/u^*} \tag{2.1}$$

$$u^* = \sqrt{\frac{\tau_w}{\rho}} \tag{2.2}$$

u^* is the friction velocity, τ_w is the shear at the walls, and y is the normal distance to the wall. We note here that in turbulent flows, the flow near the walls is divided into three layers, and those are the viscous sublayer, the buffer sublayer and the inertial sublayer. In the viscous sublayer, viscous effects dominate the inertial effects which renders the flow laminar. In the buffer sublayer, viscous effects and inertial ones are equally dominant. Meanwhile, in the inertial sublayer the viscous effects are negligible when compared to the inertial ones resulting in a turbulent flow. We note here that the y^+ serves in indicating to which sublayer a grid point belongs. A grid point

having a $y^+ \in]0, 5[$ belongs to the viscous sublayer, a grid point having $y^+ \in]5, 30[$ belongs to the buffer sublayer, and a grid point having $y^+ \in]30, 200[$ belongs to the inertial sublayer. Noting that turbulence models avoid placing the first grid point in the buffer sublayer, the transition from the viscous sublayer to the inertial one occurs at a y^+ value that ranges between 11 and 12. As previously mentioned, wall y^+ is a measure of the y^+ value of the first grid point near the walls. Following our discussion, it is preferable to have this value less than 5, so as to capture the flow in the viscous sublayer. However, we can claim that for wall y^+ value ranging between 5 and 11, the boundary layer is fairly resolved.

For our computational domain, we employed a hybrid mesh that consists of hexahedral and tetrahedral elements. We recall that investigating the characteristics of natural convection airflow is among the objectives of our study. Hence, generating an accurate solution that allows us to interpret the physical processes of our problem imposes tight constraints on the mesh employed. Therefore, we used hexahedral elements in the regions most important for the analysis of our study, and those are the shaft and the region below it. For a faster mesh generation, we used tetrahedral elements in the remaining regions. To resolve the thermal and hydrodynamic boundary layers, we clustered elements near the walls by adding inflation layers. Figures 2.2 and 2.3 display the grids in the shaft and the region around it respectively. We note here that the addition of inflation layers was performed in such a manner that kept the maximum aspect ratio acceptable. The meshing parameters and the aspect ratio, for each geometric case are summarized in Table 2.1. The maximum wall y^+ value, determined at the shaft's walls for each case, is presented in Table 2.2. By comparing the maximum wall y^+ value calculated, we notice that the highest value is 7.2. This allows us to claim that the boundary layer is fairly resolved for all cases.

Table 2.1: Mesh Parameters and Metrics

Shaft dimensions	Inflation layer	Grid size in the shaft	Number of elements	Maximum AR in the shaft	Maximum AR of the model
1m × 1m	1.5 mm	15mm	11,461,480	14	139
2m × 2m	2 mm	20 mm	12,411,944	14	141
3m × 3m	2 mm	30 mm	9,349,292	21	141
4m × 4m	2 mm	40 mm	8,449,794	28	141
5m × 5m	1.5 mm	40mm	18,452,182	38	122

AR:Aspect Ratio

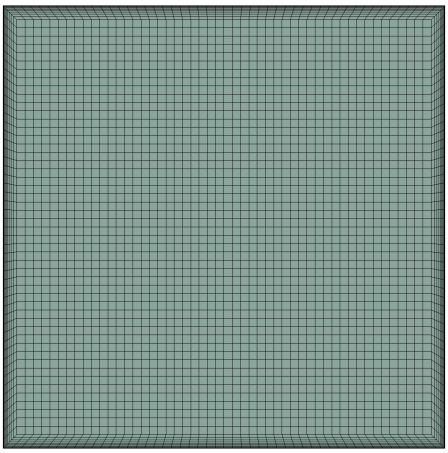

Figure 2.2: Shaft's grid

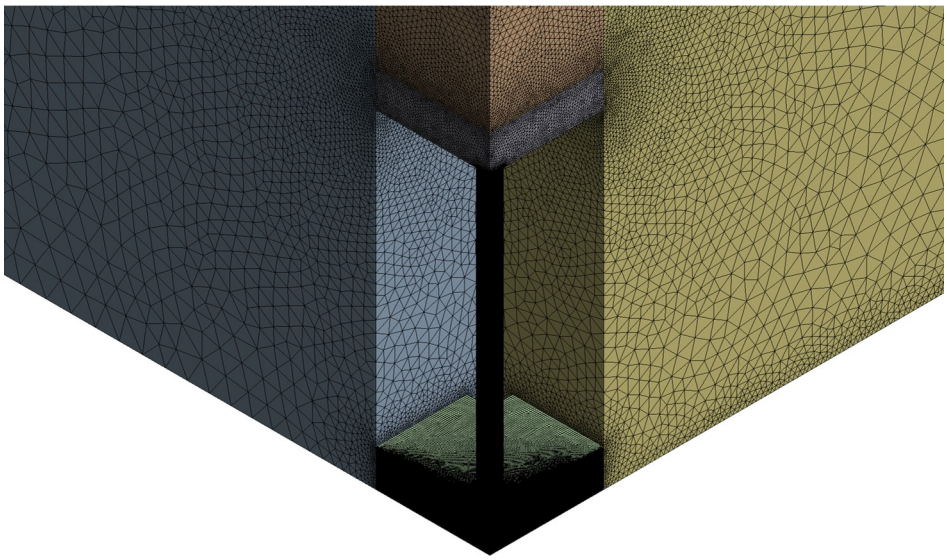

Figure 2.3: Grid of the fluid domain around the shaft

2.1.3 *Modeling and Simulation Parameters*

Given its high reliability in performing fluid flow simulations, we conducted the present study using ANSYS-Fluent where discretization is based on the finite volume method. The buoyancy force is the driving force in our flow, and it results from the variation of density in the presence of a gravitational field. We modeled air as an ideal gas having constant values for the following properties: specific heat, dynamic viscosity, and conductivity. To determine the type of the flow (laminar or turbulent),

Table 2.2: Maximum wall y^+ value at shaft's walls

	1m × 1m	2m × 2m	3m × 3m	4m × 4m	5m × 5m
05°C	2.29	3.44	3.56	3.46	2.66
10°C	3.32	4.96	4.78	4.54	3.5
15°C	3.87	5.75	5.37	5.14	4.11
20°C	4.88	6.3	6.05	5.67	4.48
25°C	4.66	6.86	6.45	6.07	4.87
30°C	4.93	7.2	6.94	6.43	5.17

Rayleigh number, given by Equation 2.3, is calculated for each case and presented in Table 2.3.

$$\mathtt{Ra} = \mathtt{GrPr} \tag{2.3}$$

$$\mathtt{Gr} = \frac{\rho_f^2 g \beta b^3 \left(T_w - T_\infty\right)}{\mu_f^2} \tag{2.4}$$

$$\mathtt{Pr} = \frac{\mu c_p}{\lambda} \tag{2.5}$$

where `Gr` is Grashoff number (ratio of buoyancy forces to viscous ones), `Pr` is Prandtl number, $\rho_f(\mathrm{kg/m^3})$ is the density of the fluid at film temperature, $g(\mathrm{m/s^2})$ is the gravitational acceleration, $\beta(1/\mathrm{K})$ is the thermal expansion coefficient, $b(\mathrm{m})$ is the shaft width, $T_w(\mathrm{K})$ is the wall temperature, $T_\infty(\mathrm{K})$ is the ambient temperature and $\mu_f(\mathrm{kg/ms})$ is dynamic viscosity of the fluid at film temperature. Film temperature is the average temperature between the walls and the ambient. We observe in Table 2.3 that the minimum Rayleigh number is 4.6×10^8, which is well above 10^5 rendering the flow turbulent [12] .

Table 2.3: Rayleigh Number

Case	1m × 1m	2m × 2m	3m × 3m	4m × 4m	5m × 5m
$\Delta T = 05°\mathrm{C}$	4.6×10^8	3.7×10^9	1.2×10^{10}	3.0×10^{10}	5.8×10^{10}
$\Delta T = 10°\mathrm{C}$	8.9×10^8	7.1×10^9	2.4×10^{10}	5.7×10^{10}	1.1×10^{11}
$\Delta T = 15°\mathrm{C}$	1.3×10^9	1.0×10^{10}	3.5×10^{10}	8.3×10^{10}	1.6×10^{11}
$\Delta T = 20°\mathrm{C}$	1.7×10^9	1.3×10^{10}	4.5×10^{10}	1.1×10^{11}	2.1×10^{11}
$\Delta T = 25°\mathrm{C}$	2.0×10^9	1.6×10^{10}	5.4×10^{10}	1.3×10^{11}	2.5×10^{11}
$\Delta T = 30°\mathrm{C}$	2.32×10^9	1.85×10^{10}	6.26×10^{10}	1.48×10^{11}	2.9×10^{11}

Turbulence modeling is commonly done using the two-equation models of the Reynolds-averaged Navier Stokes (RANS) equations. Two-equation models allow the

user to generate sufficiently accurate solutions at a reasonable computational cost. In our study, we used the shear stress transport $k-\omega$ turbulence model which is reported to have better performance than $k-\varepsilon$ models for low Reynolds number flows [30]. Wu and Lei. [31] compared the accuracy of five two-equation RANS models in predicting the solution of turbulent natural convection in a differentially heated cavity with radiation. The authors reported that the $SST\, k-\omega$ model exhibited the best overall performance. The conditions applied to the boundaries of our domain are depicted in Figure 2.4. The far field planes -side planes, top plane and ground- are treated as stationary walls that are maintained at a temperature of 25°C. Symmetry boundary conditions are assigned to the surfaces that belong to the slicing planes, and adiabatic conditions are assigned to the exterior walls of the building. For each geometric case, we studied six cases of temperature difference between the walls and the ambient. We note here that isothermal conditions are applied to the shaft's walls, and these conditions are depicted in Figure 2.4.
Moving on to the numerical settings, for the pressure-velocity coupling, we used the coupled scheme which has first been developed by Caretto et al. [32]. Pressure discretization is performed using the body force weighted scheme. The numerous schemes that have been developed for the advection terms include the first order [33] and the second order upwind schemes [34]. The prior is distinguished by having better numerical stability and boundedness than the latter. However, its shortcoming is embedded in adding an artificial diffusion term to the conservation equations which compromises its accuracy. Second order schemes, on the other hand, are reported to have better accuracy, however their boundedness and stability are not always guaranteed [30]. Knowing that our model is a physically complicated one, we started our simulations by employing first order scheme for the equations of continuity, momentum, energy, turbulent kinetic energy and specific turbulence dissipation. After convergence was reached, we switched to the second order schemes [35]

2.2 Governing Equations in dimensional form

We will start this section by presenting the general equations, in Cartesian Coordinates, that govern incompressible steady state turbulent flows, and those equations express conservation of mass, momentum, energy, turbulent kinetic energy and specific turbulent dissipation. As aforementioned, the turbulence model employed is the $SST\, k-\omega$ model which is a two-equation model based on the boussinesque hypothesis. This hypothesis establishes a linear relationship between Reynolds stresses and the mean velocity gradients.

- Conservation of mass

$$\nabla \cdot (\rho \vec{u}) = 0 \tag{2.6}$$

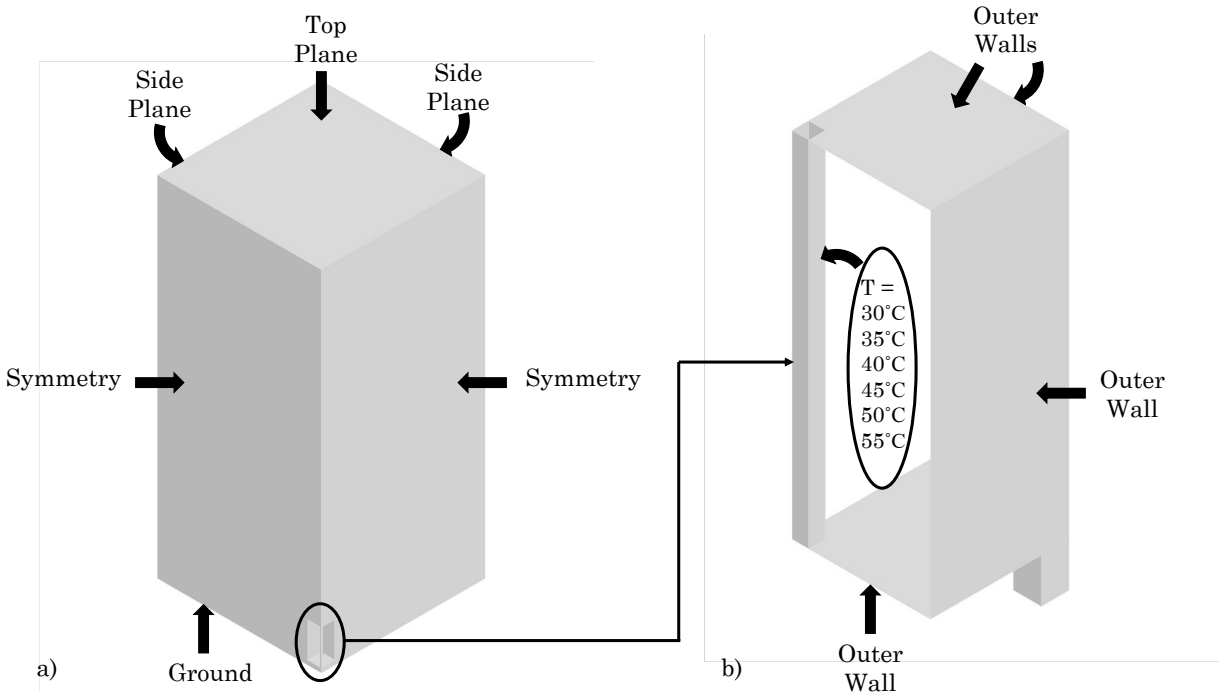

Figure 2.4: a) Schematic and boundary conditions of the computational domain b) Schematic and boundary conditions of the building

- Conservation of momentum

$$\nabla \cdot (\rho \vec{u}\vec{u}) = -\nabla p + \nabla \cdot ((\mu + \mu_t)\,\nabla \vec{u}) + \frac{1}{3}\nabla\left((\mu + \mu_t)\,\nabla \cdot \vec{u}\right) + \rho \vec{g} \tag{2.7}$$

- Conservation of energy

$$\nabla \cdot (\rho c_p \vec{u} T) = \vec{u} \cdot \nabla p + \nabla \cdot (\lambda + \lambda_t)\,\nabla T + (\mu + \mu_t)\,\Phi \tag{2.8}$$

- Conservation of turbulent kinetic energy

$$\nabla \cdot (\rho \vec{u} k) = \nabla \cdot (\mu_{eff,k} \nabla k) + P_k^* - \beta^* \rho k \omega \tag{2.9}$$

- Conservation of specific turbulence dissipation

$$\nabla \cdot (\rho \vec{u} \omega) = \nabla \cdot (\mu_{eff,\omega} \nabla \omega) + \tilde{C}_\alpha \frac{\omega}{k} P_k^* - \tilde{C}_\beta \rho \omega^2 + 2(1 - F_1)\sigma_{\omega 2} \frac{\rho}{\omega} \nabla k \cdot \nabla \omega \tag{2.10}$$

Despite its better performance near wall surfaces, the standard $k - \omega$ model [36] has been reported to be sensitive to free-stream values. To overcome this hindrance, the

standard $k-\omega$ has been modified to the SST $k-\omega$ model [37] in such a manner that the performance near the walls is not compromised, but the sensitivity to the free upstream values is abated. To start with, the SST $k-\omega$ model is the sum of the standard $k-\omega$ model multiplied by a blending function F_1 and the $k-\omega$ formulation of the standard $k-\varepsilon$ [38] model multiplied by $(1-F_1)$. The second and third modifications are pertinent to the turbulent viscosity (μ_t) and the production of turbulent kinetic energy (P_k) respectively.

$$\tilde{C}_\alpha = F_1 C_{\alpha 1} + (1-F_1) C_{\alpha 2} \tag{2.11}$$

$$\tilde{C}_\beta = F_1 C_{\beta 1} + (1-F_1) C_{\beta 2} \tag{2.12}$$

$$F_1 = \tanh(\gamma_1^4) \tag{2.13}$$

$$\gamma_1 = \text{Min}\left[\text{Max}\left(\frac{\sqrt{k}}{\beta^*\omega y}, \frac{500\nu}{y^2\omega}\right), \frac{4\rho\sigma_{\omega 2}k}{CD_{k\omega}y^2}\right] \tag{2.14}$$

$$CD_{k\omega} = \text{Max}\left(2\rho\sigma_{\omega 2}\frac{1}{\omega}\nabla k \cdot \nabla\omega, 10^{-10}\right) \tag{2.15}$$

$$\mu_t = \frac{\rho a_1 k}{\text{Max}\left(a_1\omega, \sqrt{2}S_t F_2\right)} \tag{2.16}$$

$$S_t = \sqrt{\mathbf{S_t} : \mathbf{S_t}} \tag{2.17}$$

$$\mathbf{S_t} = \frac{1}{2}\left(\nabla v + \nabla v^T\right) \tag{2.18}$$

$$F_2 = \tanh\left(\gamma_2^2\right) \tag{2.19}$$

$$\gamma_2 = \text{Max}\left(\frac{2\sqrt{k}}{\beta^*\omega y}, \frac{500\nu}{y^2\omega}\right) \tag{2.20}$$

$$\lambda_t = \frac{\mu_t c_p}{\mathtt{Pr}_t} \tag{2.21}$$

$$\mu_{eff,k} = \mu + \frac{\mu_t}{\tilde{\sigma}_k} \tag{2.22}$$

$$\mu_{eff,\omega} = \mu + \frac{\mu_t}{\tilde{\sigma}_\omega} \tag{2.23}$$

$$\tilde{\sigma_k} = \frac{\sigma_{k1}\sigma_{k2}}{\sigma_{k1} + F_1\left(\sigma_{k2} - \sigma_{k1}\right)} \tag{2.24}$$

$$\tilde{\sigma_\omega} = \frac{\sigma_{\omega 1}\sigma_{\omega 2}}{\sigma_{\omega 1} + F_1\left(\sigma_{\omega 2} - \sigma_{\omega 1}\right)} \tag{2.25}$$

$$\tag{2.26}$$

$$P_k^* = \text{Min}\left(P_k, c_1\varepsilon\right) \tag{2.27}$$
$$P_k = \tau^R : \nabla v \tag{2.28}$$
$$\varepsilon = \omega c_\mu k \tag{2.29}$$
$$\tag{2.30}$$

where y is the normal distance to the wall, $c_{\alpha 1} = 0.5532$, $c_{\beta 1} = 0.075$, $\beta^* = 0.09$, $\sigma_{k1} = 2$, $\sigma_{\omega 1} = 2$, $c_{\alpha 2} = 0.4403$, $c_{\beta 2} = 0.0828$, $\sigma_{k2} = 1$, $\sigma_{\omega 2} = 1.186$, $\mathtt{Pr}_t = 0.9$, $c_1 = 10$, $c_\mu = 0.09$, $a_1 = 0.31$

2.3 Governing equations in dimensionless form

It is a common practice in engineering applications to express the governing equations in dimensionless form. Grouping variables into dimensionless numbers simplifies the relationship between the different terms in the governing equations. It also indicates the terms that have the most significant impact on the solution, where terms of a lower order of magnitude can be discarded, thereby simplifying the equations. One very important benefit of dimensional analysis is the fact that it reduces the number of experiments needed to conduct a parametric study. Rather than changing multiple variables, it allows the user to vary a dimensionless number that is expressed in terms of the variables of interest. In other words, rather than generating a solution for a specific application, dimensional analysis allows one to generate a solution for a family of problems. In what follows, we will express our governing equations in non-dimensional form by using the non-dimensional variables expressed in Table 2.4:

- Conservation of mass

$$\tilde{\nabla} \cdot \left(\hat{\rho}\tilde{u}\right) = 0 \tag{2.31}$$

- Conservation of momentum

$$\tilde{\nabla}\cdot\left(\hat{\rho}\tilde{u}\tilde{u}\right) = -\tilde{\nabla}\hat{p} + \frac{1}{\mathtt{Gr}^{0.5}}\tilde{\nabla}\cdot\left(\left(1+\hat{\mu}_t\right)\tilde{\nabla}\tilde{u}\right) + \frac{1}{3\mathtt{Gr}^{0.5}}\tilde{\nabla}\left(\left(1+\hat{\mu}_t\right)\tilde{\nabla}\cdot\tilde{u}\right) + \frac{\hat{\rho}}{\beta\left(T_w - T_\infty\right)}\tilde{g} \tag{2.32}$$

- Conservation of energy

$$\tilde{\nabla}\left(\hat{\rho}\tilde{u}\hat{T}\right) + \frac{T_\infty}{T_w - T_\infty}\tilde{\nabla}\left(\hat{\rho}\tilde{u}\right) = \frac{gb\beta}{c_p}\tilde{u}\tilde{\nabla}\hat{p} + \frac{1}{\mathtt{PrGr}^{0.5}}\tilde{\nabla}\left(\left(1+\hat{\lambda}_t\right)\tilde{\nabla}\hat{T}\right) + \frac{gb\beta}{c_p\mathtt{Gr}^{0.5}}\left(1+\hat{\mu}_t\right)\hat{\Phi} \tag{2.33}$$

Table 2.4: Dimensionless Numbers

$\tilde{\nabla} = b\nabla$	$\hat{\rho} = \frac{\rho}{\rho_0}$	$\tilde{u} = \frac{\vec{u}}{(gb\beta(T_w - T_\infty))^{0.5}}$
$\hat{p} = \frac{p}{\rho_f\, gb\beta\,(T_w - T_\infty)}$	$\tilde{g} = \frac{\vec{g}}{g}$	$\hat{\mu}_t = \frac{\mu_t}{\mu_f}$
$\hat{\lambda}_t = \frac{\lambda_t}{\lambda_f}$	$\hat{T} = \frac{T - T_\infty}{T_w - T_\infty}$	$\hat{\Phi} = \frac{b\Phi}{g\beta(T_w - T_\infty)}$
$\hat{k} = \frac{k}{gb\beta(T_w - T_\infty)}$	$\hat{w} = \frac{wb}{(gb\beta(T_w - T_\infty))^{0.5}}$	$\hat{P}_k^* = \frac{P_k^* b}{\rho_f (gb\beta(T_w - T_\infty))^{1.5}}$
$\hat{\mu}_{eff,k} = \frac{\mu_{eff,k}}{\mu_f}$	$\hat{\mu}_{eff,\omega} = \frac{\mu_{eff,\omega}}{\mu_f}$	$\mathtt{Gr} = \frac{\rho_f^2 g\beta b^3 (T_w - T_\infty)}{\mu_f^2}$
$\mathtt{Pr} = \frac{\mu_f cp}{\lambda}$	$\beta = \frac{1}{T_f}$	$\mathtt{Ra} = \mathtt{Gr}\,\mathtt{Pr}$

- Conservation of turbulent kinetic energy

$$\tilde{\nabla}\left(\hat{\rho}\tilde{u}\hat{k}\right) = \frac{1}{\mathtt{Gr}^{0.5}}\tilde{\nabla}\left(\hat{\mu}_{eff,k}\tilde{\nabla}\hat{k}\right) + \hat{P}_k^* + \beta^*\hat{\rho}\hat{k}\hat{w} \tag{2.34}$$

- Conservation of specific turbulent dissipation

$$\tilde{\nabla}\left(\hat{\rho}\tilde{u}\hat{w}\right) = \frac{1}{\mathtt{Gr}^{0.5}}\tilde{\nabla}\left(\hat{\mu}_{eff,\omega}\tilde{\nabla}\hat{w}\right) + \tilde{C}_\alpha\hat{w}\hat{P}_k^* + \tilde{C}_\beta\hat{\rho}\hat{w}^2 + 2\left(1 - F_1\right)\sigma_{w2}\tilde{\nabla}\hat{k}\tilde{\nabla}\hat{w} \tag{2.35}$$

Chapter 3

Results and Discussion

In this chapter, we discuss the impact of the shaft size and temperature difference on flow separation at the entrance of the shaft. We also analyze the profiles of the axial velocity at different elevations. This is followed by interpreting the profile of the wall heat flux rate and displaying the centerline velocity of the 1m × 1m shaft. Moreover, we present, for each geometric case, the isotherm plots at three elevations in the shaft. In addition to displaying mass flow rate contours, we show a plot of the mass flow rates and wall heat flux rates as a function of shaft size and temperature difference. This section includes a Nusselt Number correlation in terms of a modified Rayleigh number. Furthermore, it contains two subsections in which we validate and verify our results.

3.1 Recirculation

3.1.1 *Fixed Shaft Size*

Figures 3.1 and 3.2 display the streamline plots at the entrance of the shaft. In Figure 3.1, we reveal the impact of the temperature difference on the velocity field by maintaining the shaft size constant and equal to 1m × 1m. We observe that recirculation occurs for all cases of temperature difference for this shaft. In their studies, Naylor et al [20] and Lakkis and Moukalled [19] reported that flow separation occurs at the entrance of the channel in natural convection flows when Grashoff number is sufficiently high. A small Grashoff number induces low velocities allowing the flow to enter without separation. High Grashoff numbers imply stronger buoyancy forces and consequently higher velocity magnitudes. When air is dragged into the shaft, it experiences a sudden contraction where the velocity magnitude increases. Consequently, a region of negative pressure is formed near the walls, and this results in flow separation.

Flow reattachment occurs when the buoyancy forces overcome the pressure gradient effects, and we note here that the shaft's size and temperature are the key variables that influence the reattachment length in our study. However, we observe in Figure 3.1 that the reattachment length is almost the same (0.8m) for all cases of temperature difference, and as such the impact of the shaft's temperature on the vertical extent of the recirculation zone is negligible. At a higher wall temperature, the flow will enter the shaft at a higher velocity where we would expect a delay in flow reattachment. However, with higher Grashoff numbers are associated not only higher velocities but also stronger buoyancy forces. Thus, the increase in the buoyancy force weighs the increase pressure gradient that results from higher velocity magnitudes. Hence, the reattachment length remains almost unchanged as the shaft's temperature increases.

3.1.2 *Fixed Temperature Difference*

In Figure 3.2, we present the impact of the shaft's size on the flow by maintaining the temperature difference equal to 5°C . We notice that for each geometric case, flow separation occurs when the temperature difference between the ambient and the wall is maintained at 5°C. Since this temperature difference corresponds to the minimum `Gr` for each shaft size, we can claim that recirculation occurs for all remaining cases covered in this study. As the shaft's size increases, the reattachment length increases despite the decrease in the velocity magnitude. At a constant temperature difference, the boundary layer in all cases is subjected to the same conditions rendering the impact of the shaft's size on the buoyancy force insignificant. The delay in the reattachment length can be associated with the stronger inertial forces in larger shafts. In other words, as the shaft's size increases, Reynolds number, which is a measure of the inertial forces to the viscous ones, increases. Stronger inertial forces result in larger pressure gradient effects. The increase in the reattachment length is a consequence of the unaffected buoyancy forces and increased pressure gradient effects. In short, the larger the shaft's size is, the more inviscid the flow and the larger the reattachment length are.

3.2 Velocity Profiles

3.2.1 *Fixed Shaft Size*

Figure 3.3 displays the profile of the average Z velocity along a cross section in the 3m × 3m shaft at four different elevations -0.5 m, 3 m, 6 m and 30 m- for all cases of temperature difference. We note here that the velocity profiles vary between different elevations in such a manner that does not violate the continuity equation, where the mass flow rate across all cross sectional planes should remain unchanged.

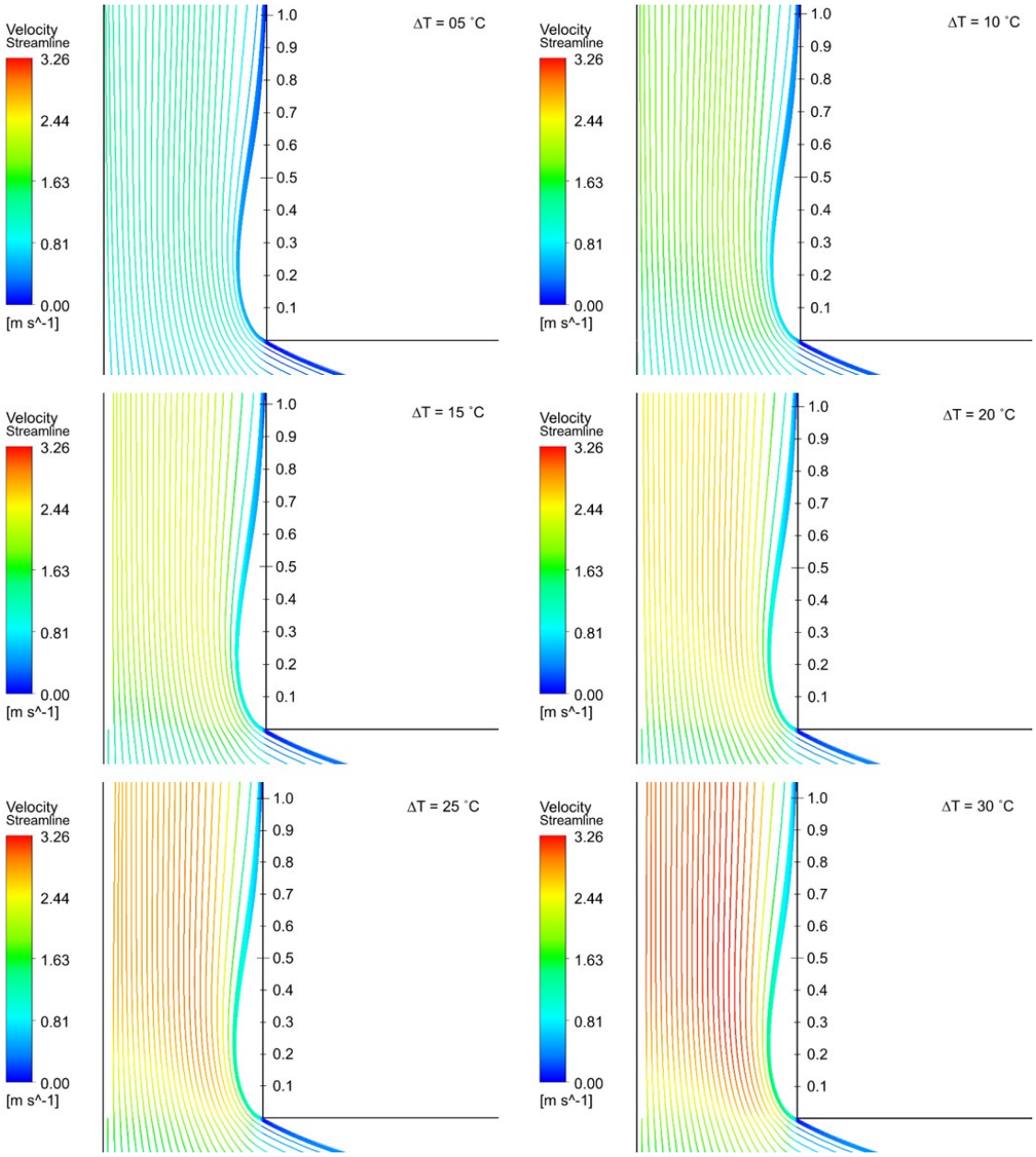

Figure 3.1: Impact of temperature difference on flow separation in the 1m × 1m shaft

The blue dotted curve corresponds to the velocity profile at an elevation of 0.5 m. The velocity near the walls decreases until it reaches a certain minimum. As we move away from the walls, the velocity increases to maximum beyond which it slightly decreases and reaches a plateau. We note here that the recirculation zone in the 3m × 3m shaft

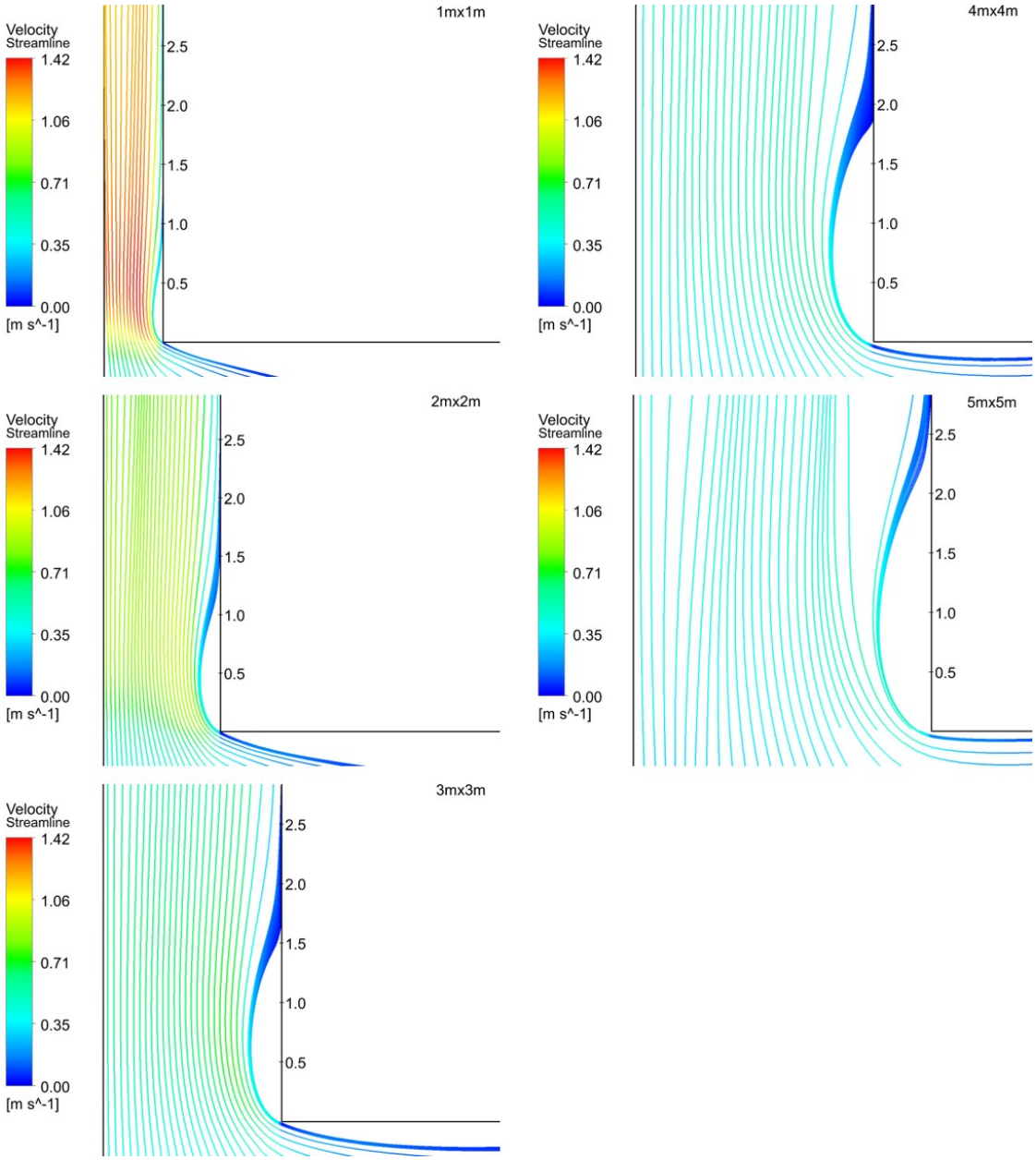

Figure 3.2: Impact of shaft size on flow separation for a temerature difference of 5°C

extends to an elevation of 1.8 m. Thus, at an elevation of 0.5 m, the flow is still in the recirculation zone where air adjacent to the walls descends.
At an elevation of 3 m (dashed-dotted orange curve), the velocity increases continuously as we move farther away from the walls and reaches its maximum velocity in

the core region of the shaft. At this elevation, the flow is reattached, and air near the walls rises. However, air is not been sufficiently heated which yields smaller velocities near the walls than in the core.
At elevations of 6 m (dashed gray curve) and 30 m (continuous yellow curve), we notice that the velocity of air near the walls increases due to the increase in its temperature and thus stronger buoyancy forces. For mass conservation to be satisfied, the increase in velocity near the walls should be compensated by a decrease in the core. The profile at an elevation of 6 m is characterized by being almost uniform where the velocity near the walls is close to that in the core. Meanwhile, the velocity profile at an elevation of 30m is distinguished by having its maximum near the walls. We note here that increasing the temperature difference yields higher velocities at all planes, but it does not have much of an impact of the shape on the velocity profile.
Figure 3.4 shows the Z velocity profiles at the following elevations: Z = 15 m, Z = 20 m, Z = 25 m, Z = 30 m. The velocity profiles at the four elevations are similar and have their maximum values near the walls. It is important to note here that at higher elevation, the maximum velocity is reached at a farther distance from the walls than at lower elevations. This is in accord with the findings of Habib et al. [7] who attributed this to the gradual increase in the boundary layer thickness.

3.3 Variation of wall heat flux

3.3.1 *Fixed Shaft Size*

In Figure 3.5, we present, for each geometric case, the impact of changing the temperature difference on the profile of the wall heat flux rate. We observe here that for a fixed shaft size, the profile of the wall heat flux rate is similar for the six cases of temperature difference. However, it differs as we change the shaft's size. The thermal and velocity fields are the key players in determining how heat is transferred between the walls and air. As the temperature of air near the walls increases, its tendency to absorb heat decreases and consequently heat transfer decreases. On the other hand, as the velocity of air near the walls increases, heat transfer increases as a result of stronger convection effects. Since in our study increasing air temperature is coupled with increasing its velocity, we can infer from the profiles of the wall heat flux rate which field -thermal or velocity- dominates the flow. We will link the variation of the wall heat flux rate with our previous discussion on the velocity profile.
As shown in Figure 3.5, the flow in the shaft could be divided into four regions. The first region corresponds to the entrance of the shaft where the heat flux rate increases until it reaches a local maximum. We associate this increase to the presence of a recirculation zone where cold air descends near the walls. In this zone, air at higher elevations has a lower temperature than air at lower elevations, and thus, as

it moves downwards, it absorbs less heat. The second region is characterized by a decreasing heat flux rate. As the flow is reattached, air near the walls rises, and it constantly absorbs heat. Thus, its temperature and velocity increase. We recall here that in this region, the velocity of air near the walls is smaller than that in the core as shown in Figure 3.3. The decreasing profile of the heat flux rate in the second region despite the increase in velocity magnitudes of air near the walls allows us to infer that the thermal field dominates the flow in the second region. In the third region, which is characterized by having an almost uniform velocity profile, we notice that the variation in the heat flux rate is slight. We can deduce here that the thermal and velocity fields are equally dominant, where the increase in temperature counteracts the increase in velocity. As for the fourth region, the heat flux rate increases for all cases except for the 1m $\times$ 1m shaft. As previously explained, in the fourth region the velocity profile near the walls has higher values than that in the core. The increase in the heat flux rate albeit the increase in the temperature of air near the walls implies a dominant velocity field.
We finally point out here that for a fixed shaft size, the profile of the wall heat flux rate becomes steeper as we increase the shaft's temperature. We mainly attribute this to the stronger convection effects that result from increasing the shaft's temperature.

3.4 Centerline Velocity

In our discussion on the wall heat flux rate, we alluded to the almost uniform heat flux rate in the fourth region of the 1m $\times$ 1m shaft. This might suggest full development in this region. For this purpose, we preent in Figure 3.6, the centerline velocity profile in the 1m $\times$ 1m shaft for all cases of temperature difference. We observe here that the centerline velocity increases at the entrance until it reaches a maximum, after which it continuously decreases. The increase at the entrance is attributed to the presence of a recirculation zone. The downward movement of air near the walls should be compensated by an increase in the velocity in the core, and this is why the centerline velocity increases in the region where recirculation occurs. As aforementioned, when the flow reattaches, the velocity near the walls increases continuously, which results in a continuous decrease in the centerline velocity. The fact that the centerline velocity did not plateau for any case allows us to infer that the flow did not reach full development.

3.5 Temperature Contours

3.5.1 *Plane z=0.5m, z=3m and z=30m*

Figure 3.7 shows the impact of changing the shaft's size on the isotherm plots while maintaining the temperature difference equal to 5°C. The plots are normalized to the shaft's size. The minimum contour value, uniform step size between two consecutive contours and maximum contour values are displayed at the top. The isotherm plots are generated along three cross-sectional planes of one fourth of the shaft at elevations of 0.5 m, 3 m and 30 m. We note here that the distribution of isotherms is mainly determined by the dominant mode of heat transfer. If conduction is dominant, isotherms become more uniformly distributed, whereas if convection is dominant the isotherms become more distorted.
At an elevation of 0.5 m, the isotherms become more confined near the walls at the corner. As aforementioned, at the entrance of the shaft, recirculation zones are present. Those zones are intensified at the corner, and thus, air having lower temperature circulates near the corners. At an elevation of 3 m, we observe that the isotherms become more distributed near the corner and more confined near the walls. We attribute this to the fact that a point located in the vicinity of the corner receives heat from both walls. Meanwhile, a point located near a wall and away from the corner receives heat from one wall. The temperature contours become more uniformly distributed for all cases of shaft size at an elevation of 30 m. We associate this with the longer contact of air with the walls which is pertinent to boundary layer development. In other words, at higher elevations, heat can better propagate, by diffusion, in the direction normal to the flow.
An interesting observation can be made here on the impact of the shaft's size on the temperature contours at all elevations, where increasing the shaft's size results in clustering the isotherms near the walls. The temperature contours become more confined near the walls as the shaft's size increases as a result of the larger volume of air in the shaft. That is to say for the 5m × 5m shaft, the propagation of heat into the shaft's core requires longer contact of air with the walls than that required by the 1m × 1m shaft.

3.6 Mass Flow rate, Wall Heat Flux and Nusselt Number

In this section, we present tables of the mass flow rate (Table 3.1), wall heat flux rate (Table 3.2) and average Nusselt Number (Table 3.3) for all cases covered in this study. We also present, in Figure 3.8, the mass flow rate contours as a function of shaft size and temperature difference. We observe in this figure that the mass flow rate increases as the temperature difference and/or the shaft size increases. Increasing

the temperature difference yields higher mass flow rates as a consequence of stronger buoyancy forces and larger velocity magnitudes. Increasing the shaft's size results in increasing the cross-sectional area through which air is passing, and thus larger mass flow rates.
As for the total wall heat rate and Nusselt number, they exhibit a similar behavior where they increase as the shaft's size and/or temperature difference increases.

Table 3.1: Mass flow rate (kg/s) induced in the shaft

Shaft Size	Temperature Difference					
	5°C	10°C	15°C	20°C	25°C	30°C
1m × 1m	1.05	1.45	1.75	2.00	2.22	2.41
2m × 2m	2.86	3.94	4.78	5.47	6.08	6.61
3m × 3m	5.00	6.89	8.30	9.50	10.50	11.48
4m × 4m	7.47	10.09	12.41	13.95	15.62	17.00
5m × 5m	10.45	14.34	17.24	19.73	21.70	23.53

Table 3.2: Wall Heat Rate (kW)

Shaft Size	Temperature Difference					
	5°C	10°C	15°C	20°C	25°C	30°C
1m × 1m	1.67	4.39	7.84	11.82	16.14	20.72
2m × 2m	3.01	8.07	14.37	21.56	29.41	37.71
3m × 3m	4.50	12.04	21.22	31.59	42.90	55.10
4m × 4m	5.88	15.71	27.95	41.35	56.26	71.98
5m × 5m	7.42	19.56	34.61	52.32	70.97	91.47

Table 3.3: Nusselt Number

Shaft Size	Temperature Difference					
	5°C	10°C	15°C	20°C	25°C	30°C
1m × 1m	100	130	154	173	188	199
2m × 2m	180	239	282	315	342	363
3m × 3m	269	357	417	462	499	530
4m × 4m	351	466	549	605	654	692
5m × 5m	443	580	680	765	825	880

Figure 3.9 displays the plots of the mass flow rates and wall heat flux rates as a function of the shaft's size and temperature difference. This figure serves in providing guidelines for designing shafts having a similar configuration to the ones covered in this study. For instance, if we desire to induce a mass flow rate of 14 kg/s in a shaft maintained at a temperature of 20°C, we need a shaft whose size is 4m × 4m. Figure 3.9 allows us to predict that the total heat rate emitted by the walls would be around 41 kW.

We also present a correlation between average value of Nusselt number and the modified Rayleigh Number. The latter is expressed in the Equation 3.1. We note here that the modified Rayleigh number is used to account for the impact of the shaft's size on the average value of Nu. The coefficient of determination of the correlation expressed in Equation 3.2 was found to be 0.964. The utility of this correlation lies in allowing the user to predict the total heat that would be emitted in configurations having geometric parameters and physical settings similar to ours.

$$\mathrm{Ra_m} = \mathrm{Ra}\left(\frac{b}{H}\right) \tag{3.1}$$

$$\mathrm{Nu} = 2.21363\mathrm{Ra_m}^{0.2391} \tag{3.2}$$

3.7 Validation

As aforementioned, the authors found limited studies that investigated turbulent three-dimensional natural convection flows in an isothermally-heated open-ended duct. As such, we cannot compare our results to experimental data generated for a configuration very similar to ours. One way to go around this is to assume that the four walls of the shaft act as independent vertical plates and to calculate the total heat emitted from those walls according to empirical correlations established for vertical plates. The fact that full-development of the flow was not observed in any of the cases justifies our assumption. In 1975, Churchill and Chu [39] reported a correlation for the average Nusselt number that is valid for all Rayleigh numbers in vertical plates. Their correlation is expressed in Equation 3.3

$$\mathrm{Nu_{vp}} = \left\{0.825 + \frac{0.387\mathrm{Ra_{vp}}^{(1/6)}}{\left[1 + \left(\frac{0.492}{\mathrm{Pr}}\right)^{(9/16)}\right]^{(8/27)}}\right\}^2 \tag{3.3}$$

$$\mathrm{Ra_{vp}} = \frac{g\beta\left(T_w - T_\infty\right)L^3}{\nu\alpha} \tag{3.4}$$

We note that the characteristic length in Equation 3.4 is the length of the vertical plate which is the height of the wall (H) in our case. This is different from the characteristic

length taken in Equation 2.3 which is the size of the shaft (b). Knowing that $\mathtt{Ra}_{\mathrm{vp}}$ is independent from the shaft's size, each ΔT has one Nusselt Number for all geometries. Estimating the Nusselt number, allows us to calculate the convection heat transfer coefficient (Equation 3.5), which in turn allows us to predict the total heat rate that would be emitted from the walls (Equation 3.6).

$$\mathtt{Nu} = \frac{hL}{k} \tag{3.5}$$

$$Q_w = hA\Delta T \tag{3.6}$$

where $A = 4Hb$ (m^2) is the total area of the shaft's walls, Table 3.4 displays $\mathtt{Ra}_{\mathrm{vp}}$, $\mathtt{Nu}_{\mathrm{vp}}$ and h for all cases of temperature difference, and Table 3.5 presents the predicted values of wall heat flux rate.

Table 3.4: Rayleigh Number, Nusselt Numer and h for vertical plates

ΔT	05°C	10°C	15°C	20°C	25°C	30°C
$\mathtt{Ra}_{\mathrm{vp}}$	1.53×10^{13}	2.94×10^{13}	4.25×10^{13}	5.47×10^{13}	6.58×10^{13}	7.34×10^{13}
$\mathtt{Nu}_{\mathrm{vp}}$	2701	3347	3776	4102	4358	4519
h	2.21	2.75	3.13	3.42	3.66	3.82

Table 3.5: Predicted Wall Heat Rate

Shaft Size	Temperature Difference					
	5°C	10°C	15°C	20°C	25°C	30°C
1m × 1m	1.41	3.53	6.01	8.77	11.72	14.68
2m × 2m	2.83	7.05	12.02	17.53	23.44	29.36
3m × 3m	4.24	10.58	18.03	26.30	35.16	44.04
4m × 4m	5.65	14.11	24.04	35.06	46.88	58.73
5m × 5m	7.06	17.63	30.05	43.83	58.61	73.41

In Table 3.6, we present the percent relative difference between the predicted values (Table 3.5) of the wall heat flux rate and the calculated ones (Table 3.2). We observe that the difference increases as the shaft's size decreases, and that the error is highest for the 1m × 1m shaft. This is attributed to the fact that as the shaft's size increases, the shaft's walls have less of an influence on the fluid in the core, which increases their similarity to a flat plate. We recall that in Figure 3.7 the isotherm plots were more distributed at an elevation of 30m for the 1m × 1m shaft than for the other cases. This allows us to infer that, for this configuration, the core region of the

shaft absorbed more heat as a result of its higher proximity to all heated walls. We also observe that the absolute error increases as the temperature difference between the walls and the ambient increases. The increase in the wall heat flux rate, resulting from the increase in ΔT, yields a stronger diffusion of heat in the shaft's core. By this, the influence of the shaft's walls on the core increases, and the walls deviate from the flat plate similarity. It is important to note here that in our comparison between the predicted values and the calculated ones we disregarded the impact of the recirculation zone. Therefore, we can claim a portion of the absolute difference is attributed to the flow separation at the entrance of the shaft.

Table 3.6: Percent Relative Difference (%) between Predicted and Calculated Values

Shaft Size	Temperature Difference					
	5°C	10°C	15°C	20°C	25°C	30°C
1m × 1m	18.11	24.47	30.49	34.87	37.71	41.10
2m × 2m	6.50	14.47	19.60	23.00	25.45	28.43
3m × 3m	6.28	13.83	17.68	20.12	22.01	25.11
4m × 4m	4.07	11.40	16.28	17.95	20.00	22.57
5m × 5m	5.04	10.94	15.19	19.39	21.10	24.60

3.8 Verification

In this section, we will present our main findings as we refined the grid for the 3m×3m shaft. The first inflation layer was moved 1mm closer to the walls and the grid size was reduced in such a manner that kept the maximum aspect ratio almost unchanged. Simulations using the refined grid were performed for the following cases of ΔT: $\{05°C, 10°C, 20°C\}$. Table 3.7 displays the main meshing parameters and the percent relative difference between the coarse grid and fine gid solutions of the mass flow rate and wall heat flux rate. We observe the percent relative error of the mass flow rate ranges between 1.71% and 3.95% and the percent relative error of the wall heat flux rate ranges between 5.63% and 6.82%. In the coarse grid, the wall y^+ value ranges between 3.56 and 6.05, whereas in the fine grid it ranges between 1.72 and 2.94.

3.9 Limitations

We acknowledge that this study has some limitations which necessitate the investigation of other aspects that might affect the flow in the shaft. For instance, we neglected that impact of radiation effects on the characteristics of airflow and the total heat

Table 3.7: Percent Relative Difference (%) between Coarse and Fine Grids

3m × 3m	Inflation Layer (mm)	Number of Elements	Mass Flow Rate (kg/s)	Wall Heat Flux Rate (W)	Wall y^+ Value
Coarse -$\Delta T = 5$°C	2	9,349,292	5	4,504	3.56
Fine -$\Delta T = 5$°C	1	15,733,511	4.81	4,260	1.72
% Difference	-	-	3.95	5.73	-
Coarse -$\Delta T = 10$°C	2	9,349,292	6.89	12,041	4.78
Fine -$\Delta T = 10$°C	1	15,733,511	6.64	11,272	2.26
% Difference	-	-	3.77	6.82	-
Coarse -$\Delta T = 20$°C	2	9,349,292	9.5	31,585	6.05
Fine -$\Delta T = 20$°C	1	15,733,511	9.34	29,900	2.94
% Difference	-	-	1.71	5.63	-

emitted from the walls. Moreover, the outdoor conditions, addressed in this study, assume absence of a velocity field around the building. Furthermore, increasing the exterior temperature of the walls to the values suggested might raise some concerns in energy efficiency enthusiasts. The latter might fear degrading the indoor thermal conditions as a result of higher external wall temperature. Moreover, the method by which walls are to be heated should be studied.

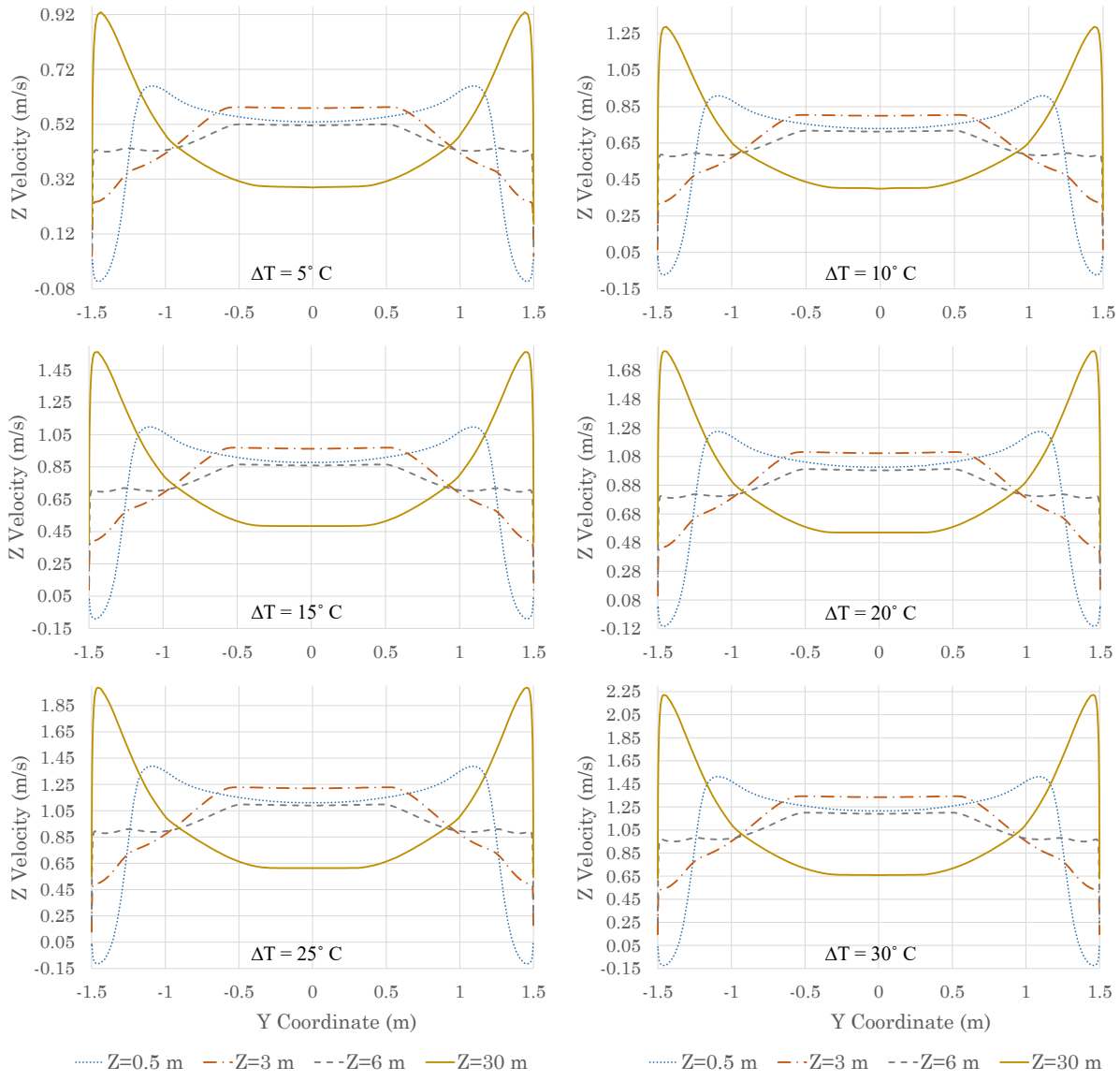

Figure 3.3: Impact of temperature difference on the velocity profiles of the 3m × 3m shaft

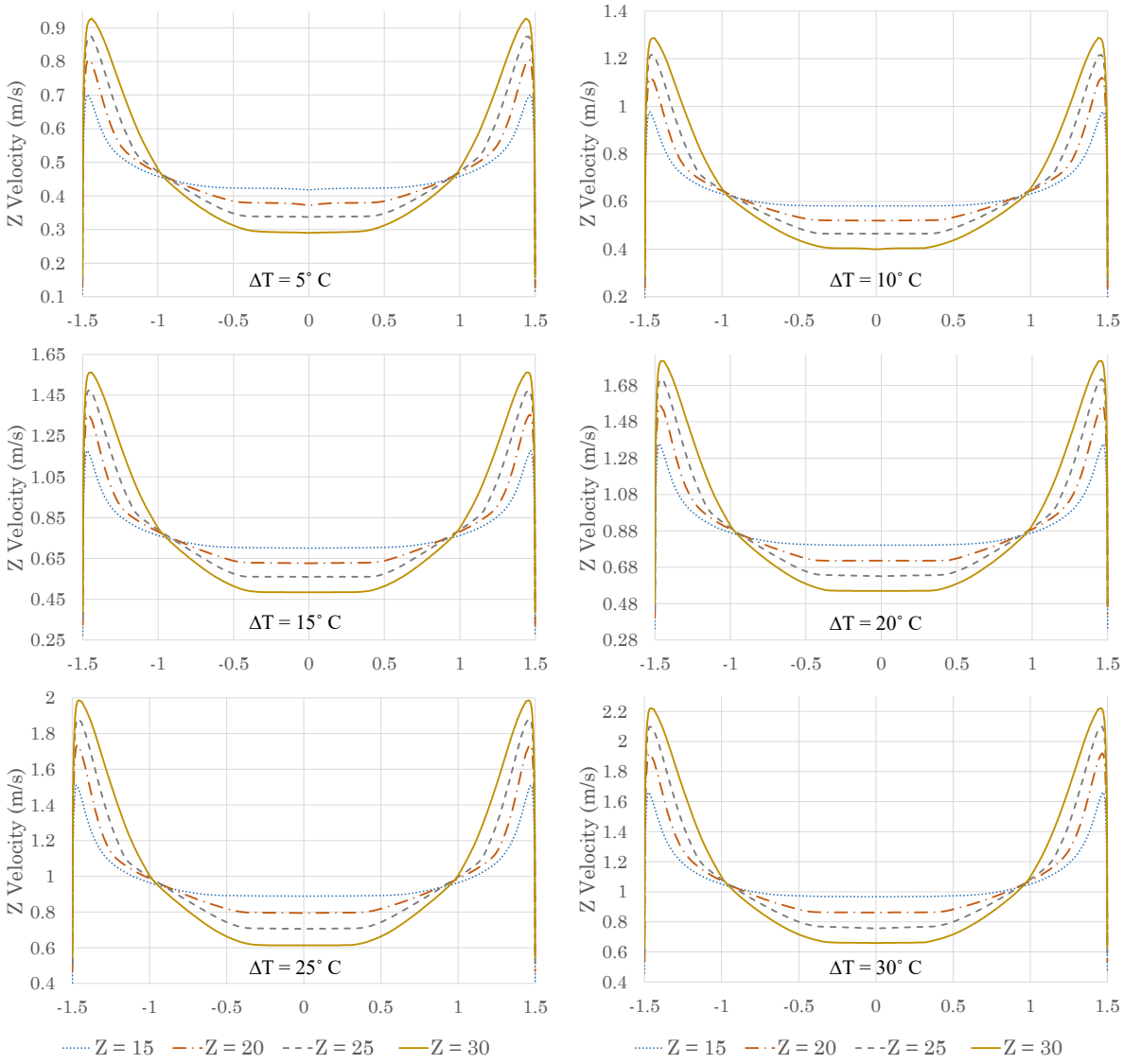

Figure 3.4: Delay in the maximum velocity for all cases of temperature difference in the 3m × 3m shaft

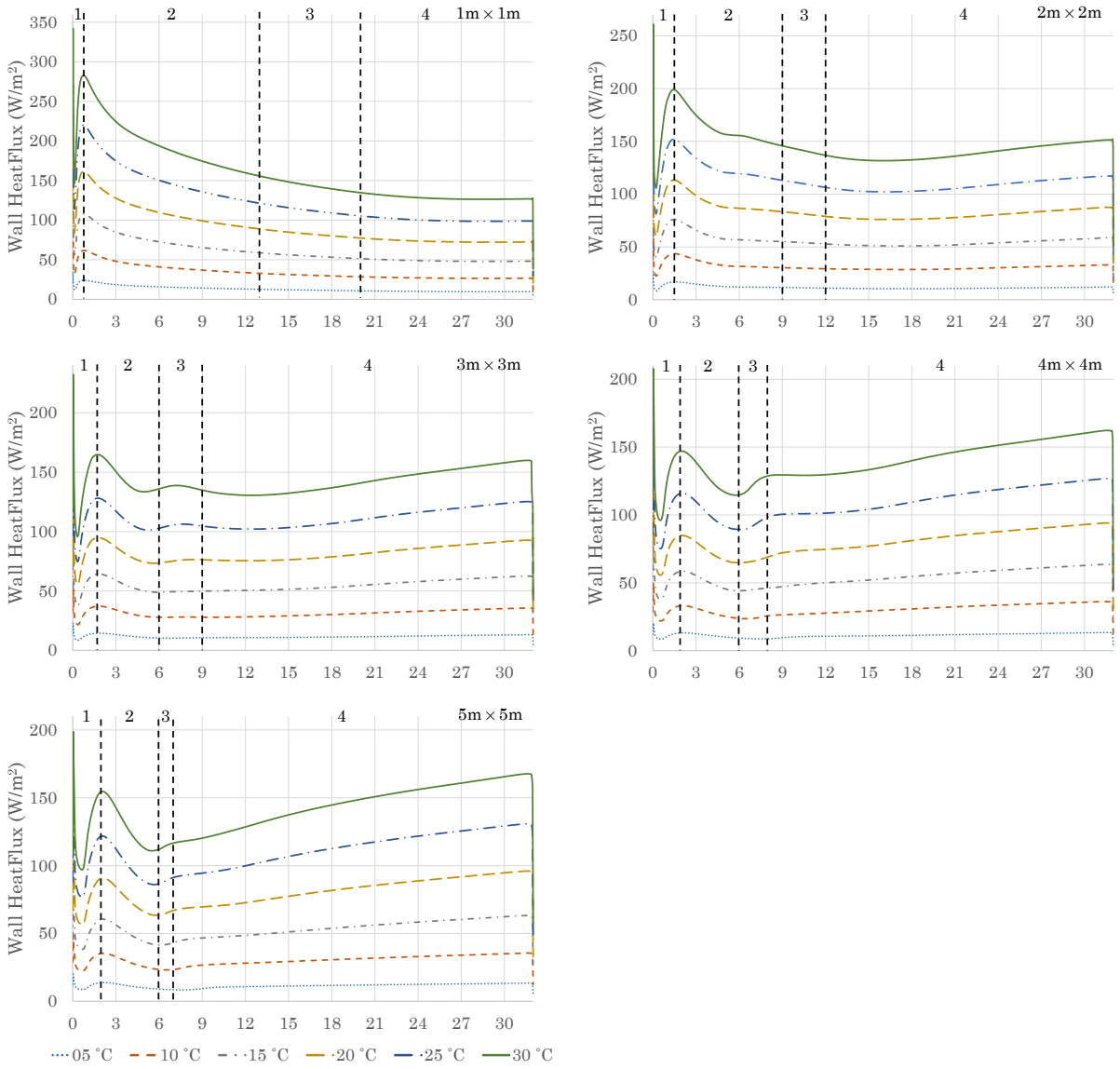

Figure 3.5: Impact of temperature difference on wall heat flux rate for all shaft sizes

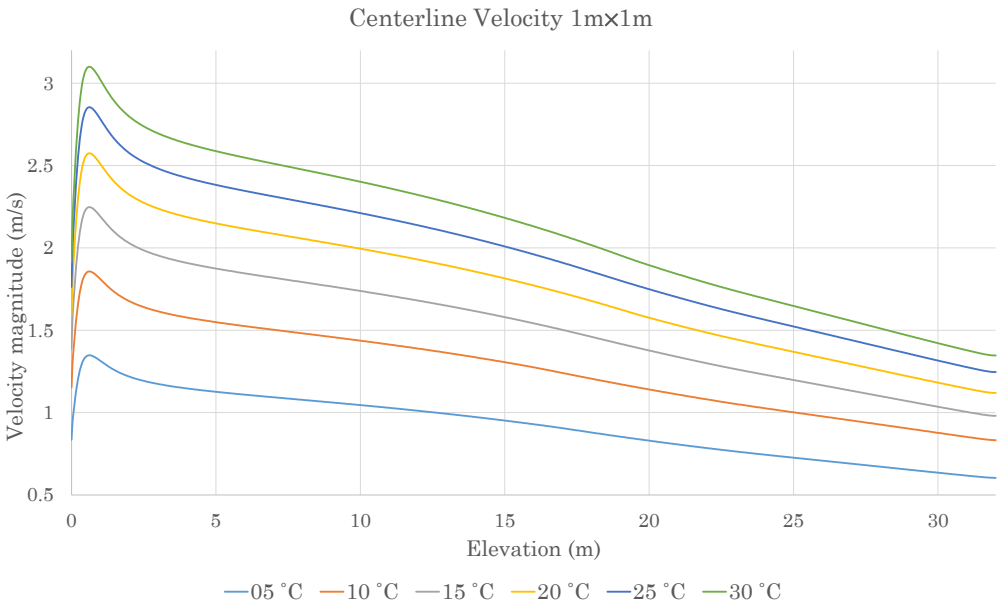

Figure 3.6: Profile of the centerline velocity for the six cases of temperature difference of the 1m × 1m shaft

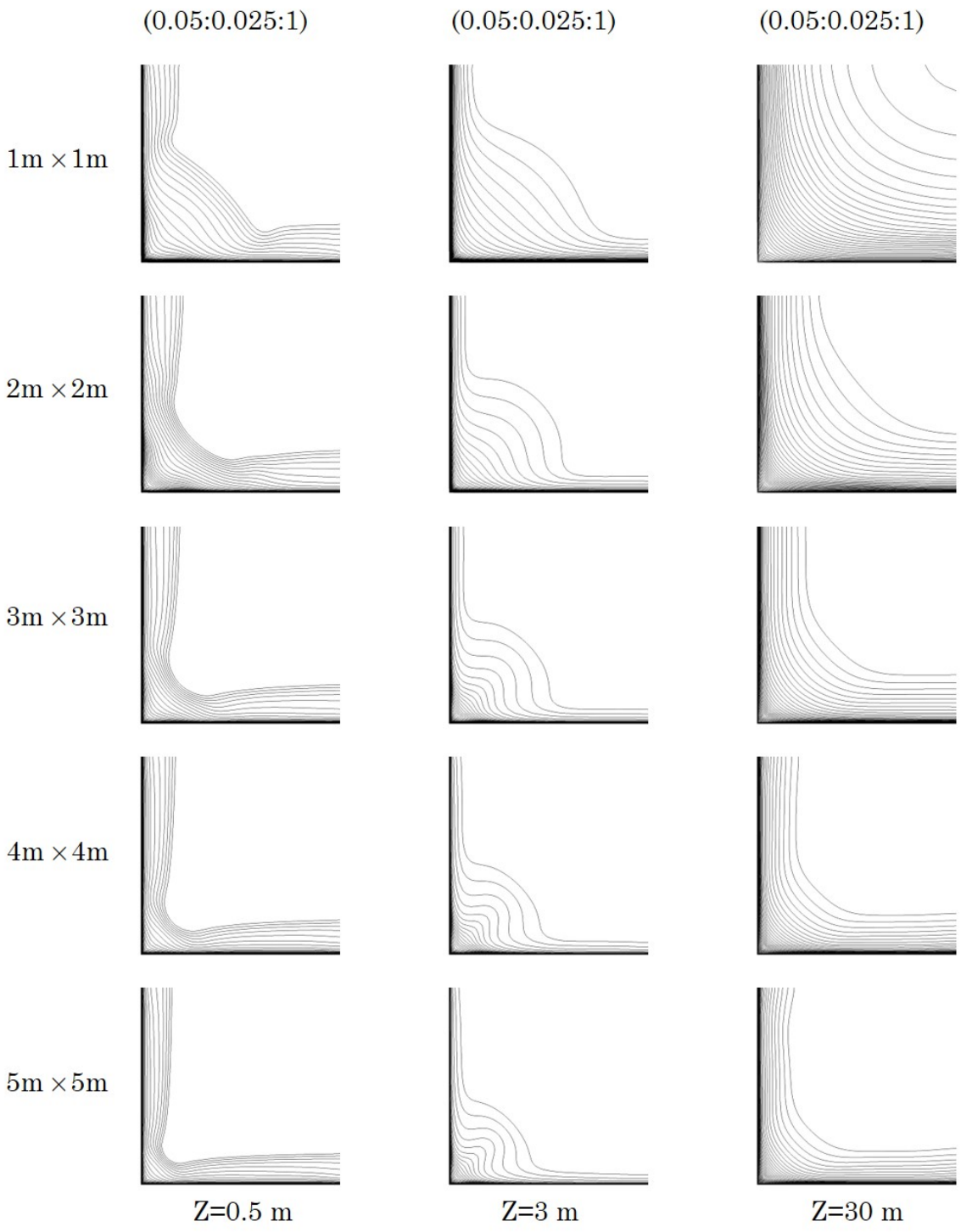

Figure 3.7: Impact of the shaft size on the isotherm plots at different cross-sectional planes in the shaft for a temperature difference of 5°C

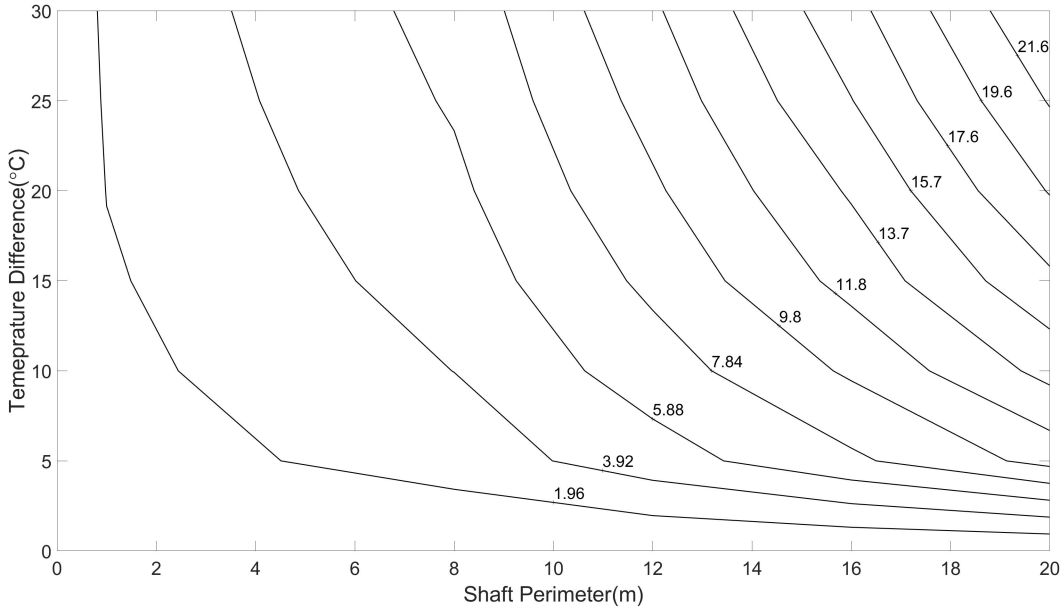

Figure 3.8: Mass flow rate contours as a function of shaft size and temperature difference

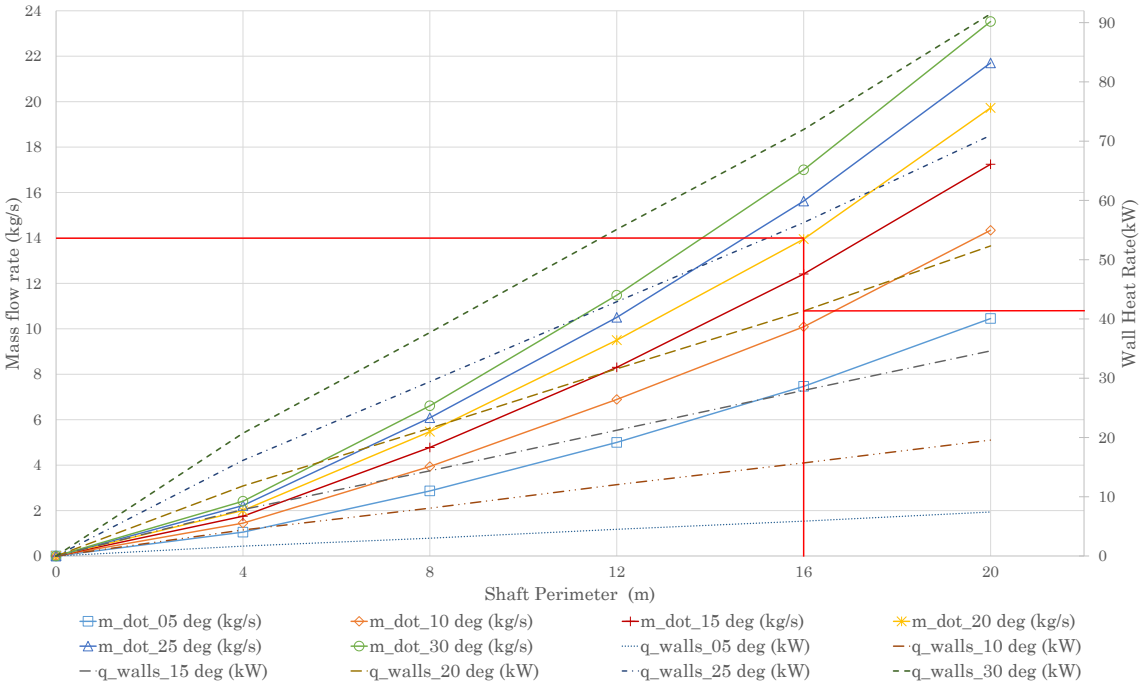

Figure 3.9: Mass flow rate and Wall heat flux plots

Chapter 4

Conclusion

A parametric study on the characteristics of turbulent three-dimensional natural convection airflow in an isothermally-heated open-ended building shaft was performed. The parameters involved in our study are the shaft size (five cases) and the temperature difference (6 cases). The maximum wall y^+ value, an indicator of how well the boundary layer is resolved, among all cases is reported to be 7.2. Our results reveal the presence of a recirculation zone at the entrance of the shaft for the 30 cases covered. Moreover, for a fixed shaft size, the impact of the temperature difference on the reattachment length is insignificant. However, the impact of the shaft size, at a fixed temperature difference, proves to be important where increasing the shaft's size yielded larger reattachment lengths. Recirculation zones appear at the entrance of the shaft as a result of the sudden contraction in the cross sectional area through which air is flowing. Flow reattachement occurs when the buoyance forces overcome the pressure gradient effects. The velocity profiles at $z = 0.5$ m, $z = 3$ m, $z = 6$ m, and $z = 30$ m of the 3m $\times$ 3m shaft are presented for all cases of temperature difference. At $z = 0.5$ m, the velocity is negative near the walls. At $z = 3$ m, the maximum velocity is attained in the core. At $z = 6$ m the velocity profile is almost uniform. At $z = 30$ m, the maximum velocity is reached near the walls. The thermal and velocity fields govern the variation of the wall heat flux in the shaft, which is divided into four regions. The first region is governed by flow separation and the second is governed by the thermal field. In the third region, the thermal and velocity fields are equally dominant, and in the fourth region, the velocity field dominates the flow. The centerline velocity for all cases of temperature difference of the 1m $\times$ 1m shaft revealed that full development of the flow was not reached for any case. In the recirculation zone, isotherms were found to be clustered near the corner. At an elevation of 3 m, the isotherms become more distributed in the vicinity of the corner and more confined near the walls. At an elevation of 30 m the isotherms become more uniformly distributed as a result of boundary layer development. Clustering of

isotherms near the walls as the shaft's size increases was observed at all elevations. For the cases addressed in our study, the mass flow rate generated in the shaft ranges between 1.05-23.53 kg/s, and the total heat rate emitted by the walls ranges between 1.67-91.47 kW.

For future work, we can develop a one dimensional model that gives a rough estimation on the mass flow rate that would be generated in the shaft. This model serves in allowing the user to determine the optimal shaft dimensions and temperature for a specific application. After those dimensions are determined, a numerical study can be performed for an in-depth analysis of its results. We can also extend this study to quantify the improvement in air quality that would result from using a building configuration similar to ours in urban areas. Moreover, we can investigate how the recirculation affects the flow in the shaft. This can be done by studying the flow characteristics in the shaft whose entrance is designed to prevent flow separation. We can also investigate the impact on the natural convection heat transfer of changing the shaft's cross-sectional area with height. In short, much work that builds up on the results of our study can be done to optimize the building configuration of our study and to improve air quality.

Bibliography

[1] M. Santamouris, "Recent progress on urban overheating and heat island research. integrated assessment of the energy, environmental, vulnerability and health impact. synergies with the global climate change," *Energy and Buildings*, vol. 207, p. 109482, 2020.

[2] U. DESA, "World urbanization prospects: United nations department of economic and social affairs," *Population Division*, 2018.

[3] A. Rahimi, A. D. Saee, A. Kasaeipoor, and E. H. Malekshah, "A comprehensive review on natural convection flow and heat transfer: the most practical geometries for engineering applications," *International Journal of Numerical Methods for Heat & Fluid Flow*, 2018.

[4] S. Pandey, Y. G. Park, and M. Y. Ha, "An exhaustive review of studies on natural convection in enclosures with and without internal bodies of various shapes," *International Journal of Heat and Mass Transfer*, vol. 138, pp. 762–795, 2019.

[5] I. Miroshnichenko and M. Sheremet, "Turbulent natural convection heat transfer in rectangular enclosures using experimental and numerical approaches: A review," *Renewable and Sustainable Energy Reviews*, vol. 82, pp. 40–59, 2018.

[6] D. Roeleveld, D. Naylor, and W. Leong, "Free convection in asymmetrically heated vertical channels with opposing buoyancy forces," *Journal of heat transfer*, vol. 136, no. 6, 2014.

[7] M. Habib, S. Said, S. Ahmed, and A. Asghar, "Velocity characteristics of turbulent natural convection in symmetrically and asymmetrically heated vertical channels," *Experimental Thermal and Fluid Science*, vol. 26, no. 1, pp. 77–87, 2002.

[8] A. Mohamad, M. A. Sheremet, J. Taler, and P. Ocłoń, "Natural convection in differentially heated enclosures subjected to variable temperature boundaries," *International Journal of Numerical Methods for Heat & Fluid Flow*, 2019.

[9] J. Bodoia and J. Osterle, "The development of free convection between heated vertical plates," 1962.

[10] H. Badr, M. Habib, S. Anwar, R. Ben-Mansour, and S. Said, "Turbulent natural convection in vertical parallel-plate channels," *Heat and mass transfer*, vol. 43, no. 1, pp. 73–84, 2006.

[11] F. Incropera and D. De Witt, "Fundamentals of heat and mass transfer," 1985.

[12] R. Boudjemadi, V. Maupu, D. Laurence, and P. L. Quéré, "Budgets of turbulent stresses and fluxes in a vertical slot natural convection flow at rayleigh ra= 10^5 and 5.4×10^5," *International journal of heat and fluid flow*, vol. 18, no. 1, pp. 70–79, 1997.

[13] A. G. Fedorov and R. Viskanta, "Turbulent natural convection heat transfer in an asymmetrically heated, vertical parallel-plate channel," *International Journal of Heat and Mass Transfer*, vol. 40, no. 16, pp. 3849–3860, 1997.

[14] A. Sarmiento, V. Soares, F. Milanez, and M. Mantelli, "Heat transfer correlation for circular and non-circular ducts in the transition regime," *International Journal of Heat and Mass Transfer*, vol. 149, p. 119165, 2020.

[15] M. Yovanovich, P. Teertstra, and Y. Muzychka, "Natural convection inside vertical isothermal ducts of constant arbitrary cross section," *Journal of thermophysics and heat transfer*, vol. 16, no. 1, pp. 116–121, 2002.

[16] Y. Muzychka and M. Yovanovich, "Laminar forced convection heat transfer in the combined entry region of non-circular ducts," *J. Heat Transfer*, vol. 126, no. 1, pp. 54–61, 2004.

[17] K. Ramakrishna, S. Rubin, and P. Khosla, "Laminar natural convection along vertical square ducts," *Numerical Heat Transfer, Part A Applications*, vol. 5, no. 1, pp. 59–79, 1982.

[18] A. Moutsoglou and M. Park, "Natural convection heat transfer in a three-dimensional duct," *Journal of thermophysics and heat transfer*, vol. 7, no. 2, pp. 369–376, 1993.

[19] I. Lakkis and F. Moukalled, "Natural-convection heat transfer in channels with isothermally heated convex surfaces," *Numerical Heat Transfer, Part A: Applications*, vol. 53, no. 11, pp. 1176–1194, 2008.

[20] D. Naylor, J. Floryan, and J. D. Tarasuk, "A numerical study of developing free convection between isothermal vertical plates," 1991.

[21] K. M. Gangawane, R. P. Bharti, and S. Kumar, "Lattice boltzmann analysis of natural convection in a partially heated open ended enclosure for different fluids," *Journal of the Taiwan Institute of Chemical Engineers*, vol. 49, pp. 27–39, 2015.

[22] F. Moukalled and I. Lakkis, "Natural-convection heat transfer in channels with isoflux convex surfaces," *Heat Transfer Engineering*, vol. 30, no. 14, pp. 1151–1165, 2009.

[23] D. Sefcik, B. Webb, and H. Heaton, "Analysis of natural convection in vertically-vented enclosures," *International journal of heat and mass transfer*, vol. 34, no. 12, pp. 3037–3046, 1991.

[24] A. G. Straatman, J. Tarasuk, and J. Floryan, "Heat transfer enhancement from a vertical, isothermal channel generated by the chimney effect," 1993.

[25] B. Zamora and A. Kaiser, "Optimum wall-to-wall spacing in solar chimney shaped channels in natural convection by numerical investigation," *Applied Thermal Engineering*, vol. 29, no. 4, pp. 762–769, 2009.

[26] I. Sadrehaghighi, *Mesh Assessment & Quality Issues*. 05 2021.

[27] P. Knupp, "Remarks on mesh quality.," tech. rep., Sandia National Lab.(SNL-NM), Albuquerque, NM (United States), 2007.

[28] H. Thornburg, "Overview of the pettt workshop on mesh quality/resolution, practice, current research, and future directions," in *50th AIAA Aerospace Sciences Meeting including the New Horizons Forum and Aerospace Exposition*, p. 606, 2012.

[29] P. ROACHE, "Perspective: a method for uniform reporting of grid refinement studies," *ASME J. Fluid Engrg.*, vol. 116, pp. 405–413, 1994.

[30] F. Moukalled, L. Mangani, and M. Darwish, "The finite volume method in computational fluid dynamics: An advanced introduction with openfoam r and matlab.[sl]: Springer international publishing, 2016.(fluid mechanics and its applications). doi: 10.1007," *Cited*, vol. 2, p. 80.

[31] T. Wu and C. Lei, "On numerical modelling of conjugate turbulent natural convection and radiation in a differentially heated cavity," *International Journal of Heat and Mass Transfer*, vol. 91, pp. 454–466, 2015.

[32] L. Caretto, R. Curr, and D. Spalding, "Two numerical methods for three-dimensional boundary layers," *Computer Methods in Applied Mechanics and Engineering*, vol. 1, no. 1, pp. 39–57, 1972.

[33] R. Courant, K. Friedrichs, and H. Lewy, "Über die partiellen differenzengleichungen der mathematischen physik," *Mathematische annalen*, vol. 100, no. 1, pp. 32–74, 1928.

[34] W. Shyy, "A study of finite difference approximations to steady-state, convection-dominated flow problems," *Journal of Computational Physics*, vol. 57, no. 3, pp. 415–438, 1985.

[35] I. ANSYS, "Ansys fluent user's guide," *Canonsburg, PA*, vol. 15317, 2011.

[36] D. C. Wilcox *et al.*, *Turbulence modeling for CFD*, vol. 2.

[37] F. R. Menter, "Two-equation eddy-viscosity turbulence models for engineering applications," *AIAA journal*, vol. 32, no. 8, pp. 1598–1605, 1994.

[38] W. P. Jones and B. E. Launder, "The prediction of laminarization with a two-equation model of turbulence," *International journal of heat and mass transfer*, vol. 15, no. 2, pp. 301–314, 1972.

[39] S. W. Churchill and H. H. Chu, "Correlating equations for laminar and turbulent free convection from a vertical plate," *International journal of heat and mass transfer*, vol. 18, no. 11, pp. 1323–1329, 1975.